Radiative properties of soot fractal superaggregates including backscattering and depolarization

Romain Ceolato, Lucas Paulien, Justin Maughan, Christopher Sorensen, Matthew J Berg

Radiative properties of soot fractal superaggregates including backscattering and depolarization

Romain Ceolato[a,], Lucas Paulien[a,b], Justin B. Maughan[c], Christopher M. Sorensen[c], Matthew J. Berg[c]

[a] *ONERA, The French Aerospace Lab, Université de Toulouse, FR 31055, France*
[b] *Laboratoire EM2C, CentraleSupélec, Université Paris-Saclay, Gif-sur-Yvette, 91192, France*
[c] *Kansas State University, Department of Physics, 1228 N. 17th St., Manhattan, KS 66506-2601 USA*

Abstract

The modeling of radiative properties of soot particles can be addressed by a number of methods. Among them, the canonical Rayleigh-Debye-Gans (RDG) theory and the Superposition T-Matrix Method (STMM) are particularly well adapted to the task. Here, both RDG and STMM are used to model the radiative properties of two types of fractal aggregates indicative of soot relevant to lidar sensing. One type, a chain-like aggregate in morphology, corresponds to low-sooting flames and is well characterized by a single fractal dimension. The other type, a superaggregate, exhibits multiple fractal dimensions and is seen in heavily sooting flames. Radiative properties such as the differential scattering cross section, total scattering cross sections, backscattering cross-sections, and linear depolarization-ratio (LDR) are calculated for a range of wavelengths from $300-1100$ nm while including the wavelength dependence of the soot refractive index. Of particular interest is that depolarization by a superaggregate is found to be approximately ten times larger than the depolarization by a chain-like aggregate and both exhibit a power-law with wavelength. Results for specific wavelengths of interest to lidar (355, 532, and 1064 nm) are tabulated for lidar applications.

Keywords: Lidar, soot, T-matrix, multispectral scattering, polarimetry

1. Introduction

The incomplete combustion of hydrocarbon fuel, biomass, and other organic matter is known to produce carbonaceous soot aggregates, *i.e.*, fractal-like clusters of nanometer-scale primary particles of carbon [1]. The primary particles, called monomers here, are quasi-spherical in shape, typically less than 50 nm in diameter, and aggregate to produce extended fractal structures up to hundreds of nanometers in size. Although their chemical composition is complex and variable due to aging processes in the atmosphere, soot aggregates generally absorb sunlight strongly. Absorption leads to positive atmospheric radiative forcing, *i.e.*, heating, and largely accounts for the well-studied nature of this class of aerosol

Email address: Romain.Ceolato@onera.fr (Romain Ceolato)

particle. Indeed, the long history of laboratory and field measurements and sophisticated computer simulations go far to provide a solid understanding for how soot absorbs and scatters light [1]. What remains less known is how certain unique structures of soot influence the radiative properties including extinction, total scattering, and backscattering in addition to polarimetric properties such as the linear depolarization ratio (LDR).

In small-scale fires, soot formation can be modeled with diffusion-limited cluster aggregation (DLCA), which yields chain-like aggregates that exhibit a fractal dimension around $D_{\mathrm{f}} \sim 1.8$. For such flames, the aggregates are relatively far apart and mechanically non-interacting; a condition known as cluster dilute in DLCA theory [2]. Below, we refer to such aggregates as "canonical DLCA aggregates." In a heavily sooting flames however, aggregates become crowded enough to (mechanically) interact in the so-called cluster dense regime of DLCA. Aggregates forming in such conditions can be envisioned as aggregates of aggregates and display a hybrid-fractal character [2, 3, 4, 5, 6, 7]. We call such aggregates "superaggregates" and they are notable because they exhibit multiple fractal dimensions and are larger in overall size than canonical DLCA aggregates.

Recent observations of soot emitted from large-scale wildfires in India and the United States show clear evidence that superaggregates are present in intense fires [8]. In [8], it is hypothesized that the large-scale of these fires produces turbulent flame structures wherein canonical DLCA aggregates become trapped in vortexes that increase the particle volume-fraction leading to enhanced aggregate growth. A laboratory study of an inverted flame in [9] and another involving a fuel-pool fire [4] appear to support this hypothesis. Considering the differences in morphology between these two types of soot aggregates, it is expected that discrepancies may exist between the true radiative properties of these particles and that calculated by simple, commonly used, approximate light-scattering models. Studying such discrepancies is of practical value as they may impact the interpretation of light scattering measurements in the field.

Polarization-sensitive lidar systems are now widely used to quantify the extent of liquid and solid-phase particles in clouds [10, 11] but are also sensitive other particulate material such as soot aerosol particles. Nonzero values of the LDR can serve as an indicator that the particles are non-spherical in shape, whereas zero values are indicative of spherical particles, *e.g.*, liquid drops. Freshly generated soot exhibits small LDR values, typically LDR $\lesssim 1\%$ [12, 13], and higher values, LDR $\gtrsim 20\%$, are seen for mineral dust [14, 15], ice [16], marine particles [15], and volcanic ash particles [17, 18]. Recently, unexpectedly large LDR between 12% and 25% have been measured for a region of the atmosphere expected to contain aged wildfire soot [19]. Other lidar field-measurements, tabulated in [20], show similar large LDR values for different soot-generating events.

In previous work [21], we show the importance of accounting for the complex fractal morphology of soot aggregates for *backscattering* calculations; that is, in contrast to simple equivalent sphere models. The results enable estimation of the principal lidar parameters for large ensembles of canonical DLCA soot fractal aggregates [22]. The intent of the present study is to investigate the radiative properties of superaggregates using the Superposition T-Matrix Method (STMM). The novelty here arises from the specific morphology of superaggregates, and in particular, a comparison of the STMM results to the popular

Rayleigh-Debye-Gans (RDG) approximation. Moreover, we consider the complete angular dependence of the radiative properties in this comparison. An extension of our results to wavelengths and quantities of practical interest to lidar applications is also presented.

2. Soot aggregate models of the study

The first of the two types of aggregates investigated here, which we call the "canonical DLCA aggregate," is typical of soot forming in relatively low-sooting flames and is characterized by the statistical scaling law :

$$N_{\mathrm{m}} = k_{\mathrm{o}} \left(R_{\mathrm{g}}/R_{\mathrm{m}}\right)^{D_{\mathrm{f}}} \tag{1}$$

where N_{m} is the number of monomers in the aggregate, k_{o} is a proportionality constant (the fractal prefactor), R_{g} is the aggregate's radius of gyration – a measure of overall aggregate size – R_{m} is the monomer radius, and D_{f} is the fractal dimension [1]. For such aggregates, typical values are $R_{\mathrm{m}} \sim 15 - 20$ nm, R_{g} can range from a few times R_{m} up to a micron, $k_{\mathrm{o}} \sim 1$, and $D_{\mathrm{f}} \sim 1.8$. In the light-scattering computations to follow, this aggregate will serve as a reference.

The other aggregate type considered, the superaggregate, can form in the latter stages of the DLCA process just before the onset of a gel [2]. This implies that the nearest distance between two aggregates is approaching the value of the radius of gyration, so that clustering between the aggregates is possible. In other words, superaggregates are aggregates-of-aggregates in flames where the aggregate density is sufficiently high to cause mechanical interactions between aggregates [2]. These superaggregates generally exhibit $D_{\mathrm{f}} \sim 1.8$ at length scales $\lesssim 0.3\,\mu$m and a $D_{\mathrm{f}} > 1.8$ at larger length scales, typically $D_{\mathrm{f}} \sim 2.6$ as shown in [2].

The specific aggregates used here are generated by the DLCA model of [23] and exhibit morphology approximately representative of canonical DLCA aggregates and superaggregates. Both types are shown as insets in Fig. 1. With knowledge of the position of each monomer, the radius of gyration of either aggregate can be calculated as:

$$R_{\mathrm{g}} = \sqrt{\frac{1}{N_{\mathrm{m}}} \sum_{i=1}^{N_{\mathrm{m}}} x_i^2} \tag{2}$$

where x_i is the distance from the i^{th} monomer center to the center of mass of the aggregate. In the following, the radius of gyration for the canonical DLCA aggregate is $R_{\mathrm{g,c}} = 220$ nm and for the superaggregate is $R_{\mathrm{g,s}} = 593$ nm while the monomer radius for either aggregate is $R_{\mathrm{m}} = 20$ nm.

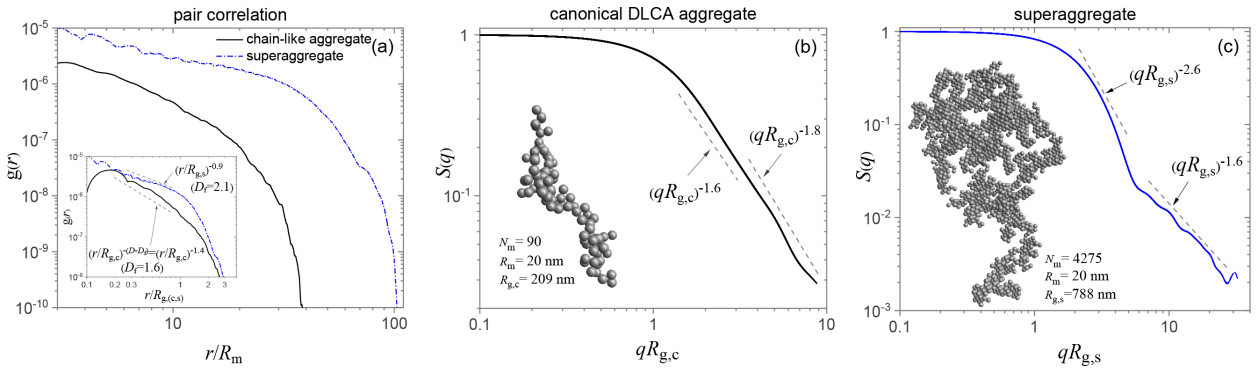

Figure 1: Pair correlation function $g(r)$ and structure factor $S(q)$ for the canonical DLCA aggregate and superaggregate. The inset in (a), where $g(r)$ is presented, shows example power-law trends following the scaling behavior described in [1] and in the text. Images of the aggregates themselves are displayed with the $S(q)$ plots in (b) and (c). Note from (b) that the canonical DLCA aggregate is approximately characterized by a limited range of fractal dimensions $D_f = 1.6$ to 1.8 while the superaggregate displays distinct power law regimes indicating multiple fractal dimensions.

To further characterize the morphology of the model aggregates, the monomer pair correlation function $g(r)$ is calculated, which is the probability of finding another monomer at a distance r from a given monomer [1]. The Fourier transform of $g(r)$ into reciprocal space, i.e., q-space, is the structure factor of the aggregate, $S(q)$ [Eq. (6) below]. As discussed in [1], the fractal-like character of the pair correlation function is given by $g(r) \sim r^{(D_f-d)}$ where $d = 3$ is the spatial dimension. When Fourier transformed, this yields the classic result that $S(q) \sim q^{-D_f}$.

Figure 1 shows these quantities along with several examples of specific power-law trends. In Fig. 1(a), $g(r)$ is presented in two ways: The main plot shows the function plotted in terms of r/R_m while the inset plot shows the same curves plotted as a function of $r/R_{g,(c,s)}$ where $R_{g,(c,s)}$ is the radius of gyration appropriate to the given aggregate. In the inset plot, we show two power laws corresponding to fractal dimensions $D_f = 1.6$ and $D_f = 2.1$ for the canonical DLCA aggregate and superaggregate, respectively. The range of $R_{g,(c,s)}$ is also slightly expanded in the inset to show further detail. Notice that the values of D_f here differ from the $D_f = 1.8$ and $D_f = 2.6$ expected from the literature [1, 2]. Next, consider Fig. 1(b) and 1(c), which shows $S(q)$ plotted as a function of $qR_{g,(c,s)}$ for each aggregate. Here again we see that multiple values for D_f apply to the the curves. In the case of the canonical DLCA aggregate, D_f is relatively well defined as being between $D_f = 1.6$ and $D_f = 1.8$. For the superaggregate, we find a different behavior, namely that two distinctly different power-law regions are present. The $D_f = 1.8$ and $D_f = 2.6$ power laws characteristic to superaggregates are not exhibited here because of the relatively small aggregate size (necessitated by limited computational resources) compared those in [2]. Nevertheless, the salient point is that the superaggregate exhibits multiple power-law regimes in $S(q)$ not seen for the canonical DLCA aggregate, and thus, the radiative properties should be affected. We investigate this question below.

3. Scattering properties of soot superaggregates

Modeling of the radiative properties of soot particles can be addressed by a number of methods. Among them are the approximate RDG theory and the numerically exact STMM [24]. The former uses scaling arguments and the reciprocal space expression of the aggregate structure in order to approximate both angle-integrated and angle-dependent radiative properties. Limitations arise from the inability of the RDG to describe internal multiple scattering among the monomers [25]. The STMM method can also provide the radiative properties of soot aggregates and is an exact solution of the Maxwell equations for any assembly of (non-intersecting) spherical particles. In the following, the STMM code of [24] is used and the results compared to the RDG approximation.

Let us fist consider an aggregate illuminated by an unpolarized incident plane wave propagating along the positive z-axis of the laboratory coordinate system. The scattering angle θ is measured between the z-axis and the vector $\mathbf{r}$, which is the observation point in the aggregate's far-field zone. Except for the study of linear depolarization below, the Stokes column vector for the unpolarized incident light is $\mathbf{I}^{\mathrm{inc}} = \left(I^{\mathrm{inc}}, 0, 0, 0\right)^{\mathrm{T}}$ where I^{inc} is the intensity of the wave. The STMM is applied to each aggregate shown in Fig. 1 to calculate the elements of the far-field scattering matrix $\mathbf{F}$, which transforms $\mathbf{I}^{\mathrm{inc}}$ into the scattered wave's Stokes vector $\mathbf{I}^{\mathrm{sca}}$ at $\mathbf{r}$. The simulation first considers a single wavelength λ in the spectral range with corresponding $m(\lambda)$ and then calculates the matrix elements. Next, the elements are analytically averaged over random aggregate-orientations and the process is then looped over wavelength in steps of $\Delta\lambda = 10\,\mathrm{nm}$ to generate the orientation-averaged scattering matrix. Because of the orientation average, either aggregate effectively constitutes a macroscopic isotropic and mirror-symmetric scattering medium. In such cases, $\mathbf{F}$ depends only on the polar scattering angle and simplifies from 14 to six independent elements [26]. In the backward direction specifically, the matrix simplifies further to only four elements as:

$$\mathbf{F}\left(\theta = \pi\right) = \begin{pmatrix} F_{11}\left(\pi\right) & 0 & 0 & 0 \\ 0 & F_{22}\left(\pi\right) & 0 & 0 \\ 0 & 0 & F_{33}\left(\pi\right) & 0 \\ 0 & 0 & 0 & F_{44}\left(\pi\right) \end{pmatrix} \tag{3}$$

The focus below is on each aggregate's differential scattering cross section, total cross sections, and LDR, which are given in terms of elements $\mathbf{F}$. The absorption and extinction cross sections C_{abs} and C_{ext}, respectively, are also provided by the the STMM calculations. We note that the broadband spectral nature of the study requires that the wavelength dependence of the refractive index m of the soot material be taken into account. From laboratory measurements and the Kramers-Krönig relation, [27] describes a soot refractive index dispersion, $m(\lambda)$, which is used here over the wavelength range $\lambda = 300 - 1100\,\mathrm{nm}$.

3.1. Differential scattering cross section

The differential scattering cross section, or phase function for unpolarized light, is expressed for incident unpolarized light as [28]:

$$\frac{\mathrm{d}C_{\mathrm{sca}}^{\mathrm{STMM}}}{\mathrm{d}\Omega}(\theta) = \frac{F_{11}(\theta)}{k^2}. \tag{4}$$

As explained in [29], the RDG description for this quantity derives from two approximations. First, that the soot monomers be in the Rayleigh-scattering size range, *i.e.*, much smaller than the wavelength. The smallest wavelength considered here is $\lambda = 300$ nm and the monomer radius is $R_\mathrm{m} = 20$ nm. As such, $\lambda \gg R_\mathrm{m}$ and this condition is well satisfied. Second, electromagnetic coupling, or "multiple scattering," between monomers is assumed negligible. When both conditions hold, the RDG description for the scattered intensity is the product of the (Rayleigh) differential scattering cross section for a single monomer, the number of monomers squared, and the structure factor, which is the Fourier transform of the aggregate structure [1, 29], *i.e.*,

$$\frac{\mathrm{d}C_\mathrm{sca}^\mathrm{RDG}}{\mathrm{d}\Omega}(q) = N_\mathrm{m}^2 k^4 R_\mathrm{m}^6 \left|\frac{m^2-1}{m^2+2}\right|^2 \left[\frac{1+\cos^2(\theta)}{2}\right] S(q). \tag{5}$$

where $q(\theta) = 2k\sin(\theta/2)$ is the scattering wave vector magnitude and $S(q)$ is related to the pair correlation function $g(r)$ [30] as:

$$S(q) = \frac{1}{N_\mathrm{m}}\left[1 + 4\pi\int_0^\infty g(r) r^2 \frac{\sin(qr)}{qr} dr\right] \tag{6}$$

Note in Eq. (5) that the term $[1+\cos^2(\theta)]/2$, expressed in terms of the scattering angle θ, is present due to the unpolarized nature of the incident light. Equation (6) assumes orientation averaging of the aggregate, and because $q = 0$ in the forward direction ($\theta = 0$), $S(0) = 1$.

Inspired by recent work in [29], we consider specifically how the STMM results compare to the RDG approximation in the forward-scattering direction. That is, we divide the angular scattering of Eq. (4) from STMM by Eq. (5) with $q = 0$ and $S(0) = 1$. The resulting quantity is denoted $\mathrm{d}C_\mathrm{sca}^\mathrm{STMM}/\mathrm{d}\Omega$ Rayleigh normalized. Also, the absorption cross section in the RDG approximation $C_\mathrm{abs}^\mathrm{RDG}$ is given in [1].

3.2. Scattering cross section

In the STMM computation, the scattering cross-section is computed as:

$$C_\mathrm{sca}^\mathrm{STMM} = 2\pi\int_0^\pi \frac{dC_\mathrm{sca}^\mathrm{STMM}}{d\Omega}(\theta)\sin(\theta)d\theta, \tag{7}$$

while in the RDG approximation it is given by [31] as:

$$C_\mathrm{sca}^{(D_\mathrm{f})} = N_\mathrm{m}^2 k^4 R_\mathrm{m}^6 \left|\frac{m^2-1}{m^2+2}\right|^2 G(kR_{\mathrm{g,(c,s)}}, D_\mathrm{f}) \tag{8}$$

where

$$G(kR_\mathrm{g}, D_\mathrm{f}) = \left[1 + \frac{4}{3D_\mathrm{f}}\left(kR_{\mathrm{g,(c,s)}}\right)^2\right]^{-\frac{D_\mathrm{f}}{2}} \tag{9}$$

and the notation $C_\mathrm{sca}^{(D_\mathrm{f})}$ is meant to differentiate Eq. (8) from $C_\mathrm{sca}^\mathrm{RDG}$. In evaluation of Eq. (8) below, a value of $D_\mathrm{f} = 1.8$ is used for the canonical DLCA aggregate and $D_\mathrm{f} = 2.6$ is used for the superaggregate. The reader should recall from Fig. 1, however, that $D_\mathrm{f} = 2.6$ is one of many choices that could be used for the superaggregate.

3.3. Results and discussion

We now investigate the light-scattering properties of the model soot aggregates. Figure 2 shows the STMM-calculated differential cross section for both aggregates, *i.e.*, Eq. (4), for a selection of wavelengths as labeled. The curves are plotted in q-space, which means a log-log scale is used and the independent variable is the dimensionless parameter $qR_{\mathrm{g,(c,s)}}$. Note that the radius of gyration is different for the two aggregates, hence $R_{\mathrm{g,c}}$ is used for the chain-like aggregate and $R_{\mathrm{g,s}}$ is used for the superaggregate. The dashed lines plot Eq. (5) in Fig. 2(a) and 2(c) and show the typical structure including a constant-scattering forward lobe when $qR_{\mathrm{g,(c,s)}} < 1$, a Guinier regime around $qR_{\mathrm{g,(c,s)}} \sim 1$, and a power-law (or laws) region reflecting the fractal character when $qR_{\mathrm{g,(c,s)}} > 1$. Because the incident light is unpolarized, the scattering curves exhibit a polarization "dip" near $\theta = 90°$ due to the Rayleigh-like scattering from the monomers. This brings the curves down from the standard $q^{-D_{\mathrm{f}}}$ power-law predicted by the structure factor discussed in [1].

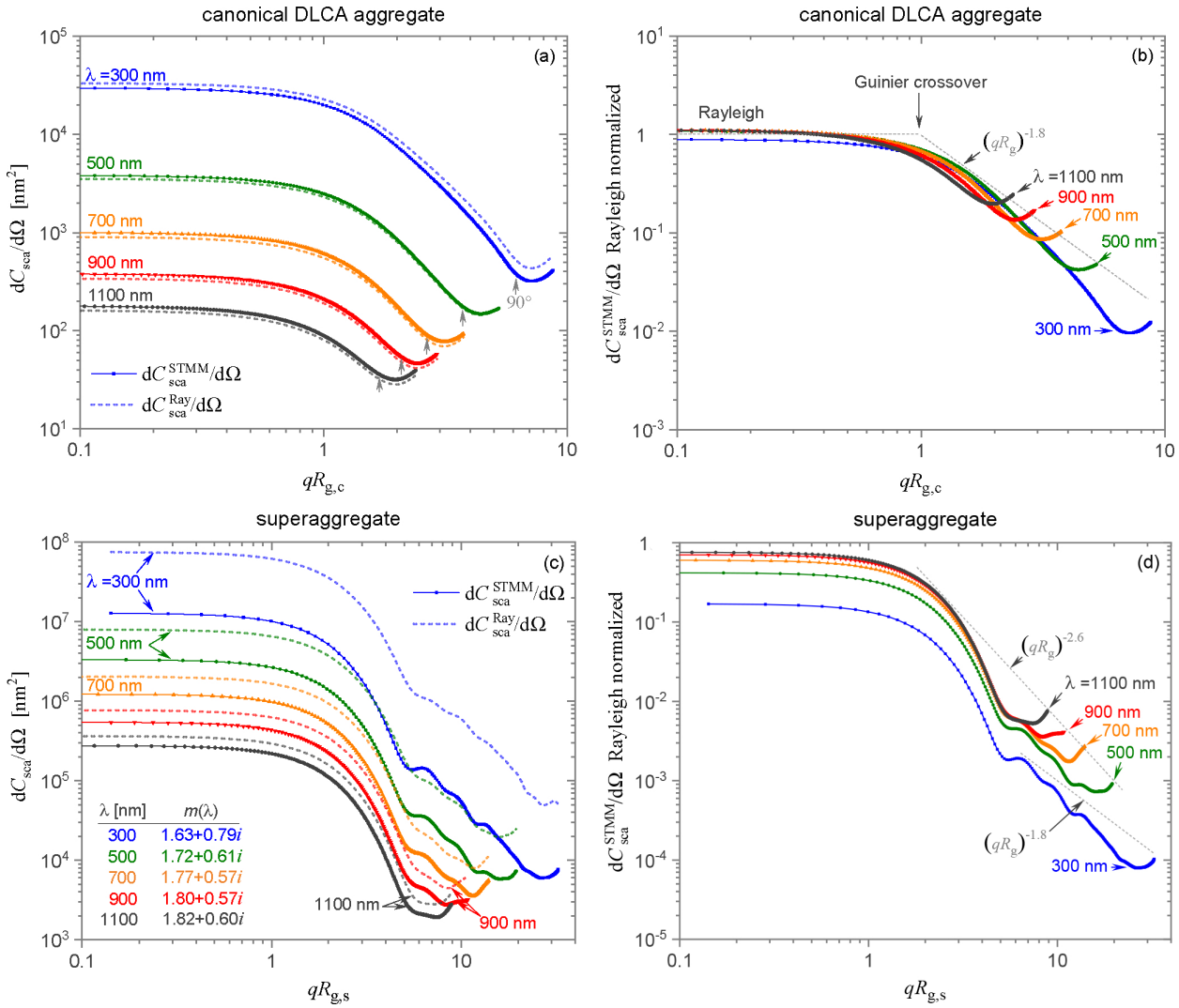

Figure 2: Angular dependence of the STMM and RDG differential scattering cross sections for the canonical DLCA aggregate and superaggregate illuminated by unpolarized light. The RDG curves, Eq. (5), are shown as dashed lines in (a). Both the STMM and RDG curves are plotted as a function of the dimensionless parameter $qR_{g,c}$ in log-log scale. The different curves correspond to different λ as labeled and markers indicate the "dip" caused by the unpolarized incident light. In plot (b) the same scattering curves have been divided by the RDG approximation for the forward scattered intensity, *i.e.*, Eq. (5) when $q = 0$. Here one can see the quasi-universality of the scattering behavior as all curves group closely together. Plots (c) and (d) show the same results for the superaggregate as a function of $qR_{g,s}$. Values for $m(\lambda)$ for the specific wavelengths used are tabulated in (c).

The power-law form of the scattering is further revealed in Fig. 2 by normalizing each STMM curve by the RDG approximated forward-scattering, Eq. (5) with $q = 0$, and the result is shown in Fig. 2(b) and Fig. 2(d) for both aggregates. For the canonical DLCA aggregate, Fig. 2(b), this normalization brings the different-wavelength curves together within approximately 10% spread from one, revealing that Eq. (5) does well to describe the forward-scattered intensity for *this* aggregate. A similar result is seen in Fig. 2(d), except with a

greater departure from one. Thus, Eq. (5) is less effective at describing the superaggregate's forward scattering.

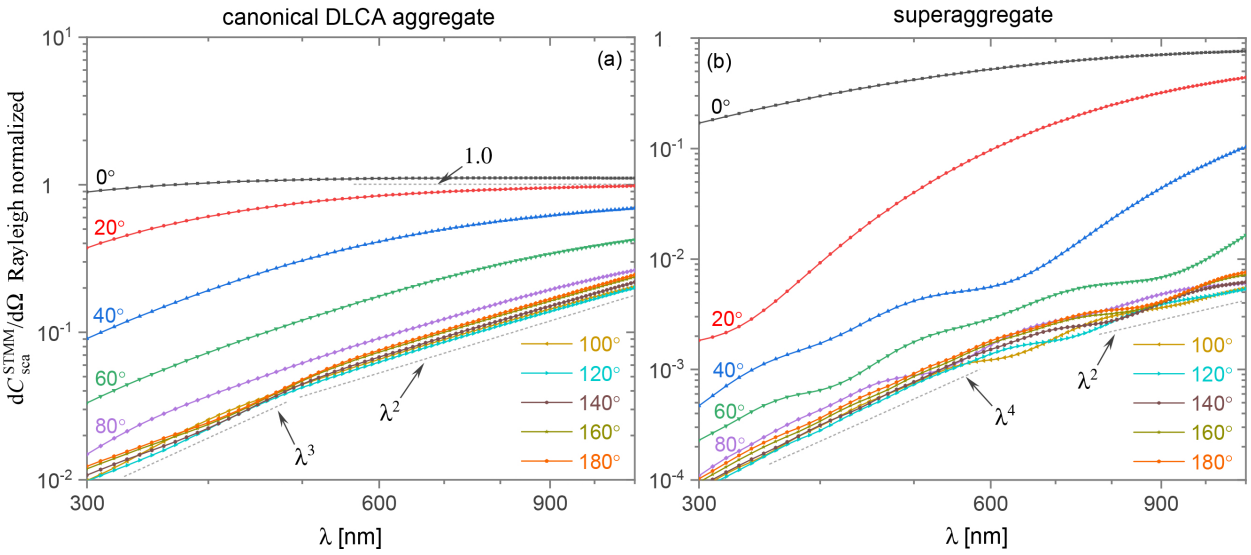

Figure 3: Rayleigh-Debye-Gans normalized differential scattering cross section as a function of λ. Each curve corresponds to a specific scattering angle as labeled. Note the quasi-invariance of the curves with scattering angle beyond $\theta \approx 80°$.

A different comparison of the STMM angular scattering with RDG is shown in Fig. 3. Here, specific scattering angles ranging from $\theta = 0°$ to $\theta = 180°$ are selected and the Rayleigh normalized differential scattering cross sections are then plotted as a function of λ. In accord with Fig. 2(b) and 2(c), good agreement with RDG is seen for forward scattering, followed by increasing degrees of departure from RDG for increasing scattering angles. However, the departure appears comparatively invariant with scattering angle beyond approximately $\theta \gtrsim 80°$, as seen by the grouping of the curves. Moreover, the trend for these angles show power laws in λ as indicated.

The wavelength dependence of the scattering and extinction cross sections for each type of aggregate are shown in Fig. 4. In general, the canonical DLCA aggregate displays good agreement with RDG across the spectral range, whereas the superaggregate departs more, especially for the UV/VIS region. Greater disagreement between STMM and RDG is seen as λ *decreases*. We suspect that this behavior is likely a consequence of refraction within the monomers. That is, as λ decreases, the field within a given monomer will increasingly depart from the uniform-field approximation underpinning RDG theory. Notice that this interpretation suggests that the disagreement (with decreasing λ) should occur regardless of the aggregate morphology. Yet, the disagreement is stronger in Fig. 4 for the superaggreagate, which may be due to the larger number of monomers. There may also be effects due to electromagnetic coupling between mononmers, which would be expected to depend on the aggregate structure. In any case, we conclude that RDG should be used with care, especially for large aggregates.

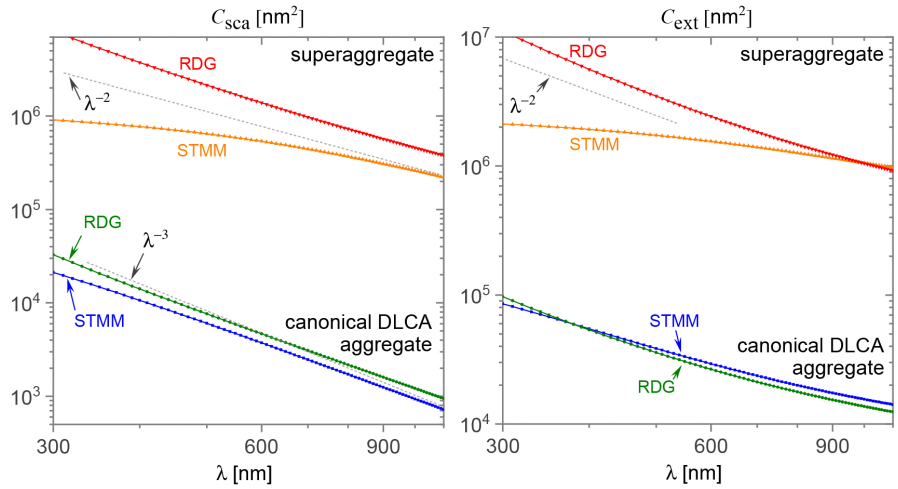

Figure 4: The STMM-calculated scattering and extinction cross sections, C_{sca} and C_{ext}, respectively, as a function of λ for the canonical DLCA aggregate and superaggregate. Comparisons to the RDG approximations for the cross sections are shown. Note that RDG agrees well with the STMM calculations for the canonical DLCA aggregate but less well for the superaggregate.

4. Backscattering and depolarization

Lidar systems enable the vertical profiling of atmospheric aerosols through the measurement of lidar-relevant radiative properties including backscattering and polarization, e.g., see [32]. Thus, to connect our study to a topic of practical interest, we extend our STMM calculations to these lidar quantities, namely the backscattering cross section and the linear depolarization ratio.

4.1. Backscattering cross section

The differential scattering cross section evaluated in the backscattering direction, $\theta = 180°$ or $q = 2k$, is called the backscattering cross section below, and is typically denoted C_π for ease of notation. In the STMM computation, C_π is expressed as:

$$C_\pi^{\mathrm{STMM}} = \frac{\mathrm{d}C_{\mathrm{sca}}^{\mathrm{STMM}}}{\mathrm{d}\Omega}(\theta = \pi) = \frac{F_{11}(\pi)}{k^2}, \tag{10}$$

while in the RDG approximations it is given in terms of Eq. (4) as

$$C_\pi^{\mathrm{RDG}} = \frac{\mathrm{d}C_{\mathrm{sca}}^{\mathrm{Ray}}}{\mathrm{d}\Omega}(q = 2k). \tag{11}$$

4.2. Linear depolarization ratio

The linear depolarization ratio (LDR) expresses the ratio of the crossed-polarized to parallel-polarized component of the backscattered intensity. That is, LDR = 0 means that the backscattered light is (linearly) polarized in the same direction as the incident light. An LDR = 1 means that two orthogonal polarizations have equal intensity. This quantity

is useful because it is sensitive to the shape of the aerosol particles [33, 26, 34, 35] and is defined from **F** above as [22]

$$\mathrm{LDR} = \frac{F_{11}(\pi) - F_{22}(\pi)}{F_{11}(\pi) + F_{22}(\pi)}. \tag{12}$$

Note that although the angular scattering behavior studied in Fig. 2 and Fig. 3 are for unpolarized incident light, the scattering matrix also describes backscattering of parallel or perpendicular incident light leading to the depolarization measure, Eq. (12).

4.3. Results and discussion

The LDR and C_π are shown in Fig. 5 for both aggregate types. By definition, RDG yields an LDR of zero because each monomer is treated in the independent-scattering limit (more explanation below). Thus, there is no RDG comparison to be made here. Both aggregates exhibit an approximate λ^{-2} power law, with the superaggregate holding less well to this power-law. The same wavelength trend is also seen for C_π. Values of the LDR for the canonical DLCA aggregate vary from $0.1 - 2\%$, which is expected for soot of this fractal dimension. However, the superaggregate shows roughly an order of magnitude larger LDR values across the wavelength range. Finally, specific values from these plots are reported in Table 1 for commonly used lidar wavelengths.

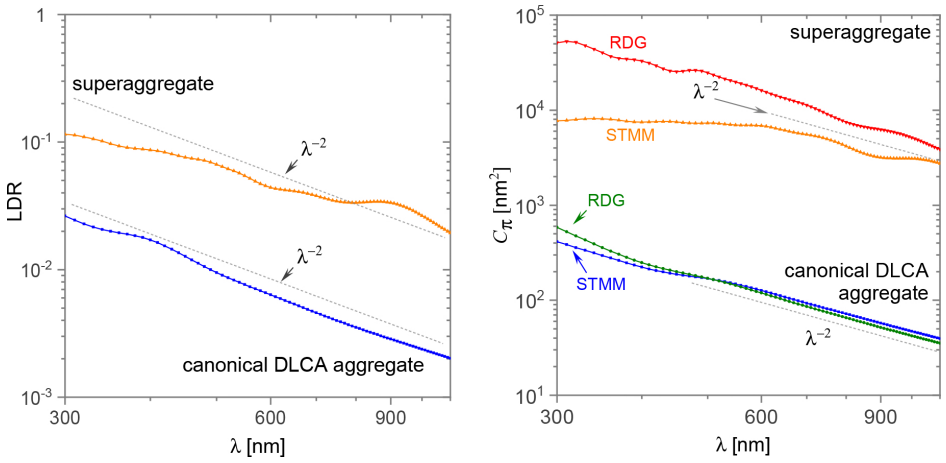

Figure 5: Wavelength dependence of the linear depolarization ratio, LDR, and backscattering cross section, C_π, as calculated by STMM and RDG for the canonical DLCA aggregate and superaggregate. Note that both quantities generally follow a λ^{-2} power law for a portion of the spectral range.

canonical DLCA aggregate				
λ [nm]	C_{sca} [nm^{2}sr^{-1}]	C_{ext} [nm^2]	C_π [nm^2]	LDR [%]
355	14277	66105	286.53	1.970
532	5139.5	35030	155.82	0.8190
1064	790.70	14602	41.965	0.2130

superaggregate				
λ [nm]	C_{sca} [nm^{2}sr^{-1}]	C_{ext} [nm^2]	C_π [nm^2]	LDR [%]
355	794770	2.0133×10^6	8068.3	9.4865
532	597570	1.6732×10^6	7127.1	5.8921
1064	232920	1.0012×10^6	2935.7	2.1657

Table 1: Values of the cross sections, C_{sca}, C_{ext}, C_π, and the LDR calculated with the STMM for the canonical DLCA aggregate and superaggregate at common lidar wavelengths.

Of specific interest for lidar is C_π. The canonical DLCA aggregate shows good agreement with RDG, Eq. (11), and an overall λ^{-2} power law is exhibited toward the IR spectral region. The agreement between RDG with STMM degrades for the superaggregate and the power-law trends are different. The departure from RDG is more pronounced for superaggregates because the monomers are, on average, more coupled for a given wavelength, *i.e.* more monomers are in each other's near-field zone. In addition to this, at smaller wavelengths, there is more refraction within a given monomer and this causes further disagreement with the RDG approximation.

The LDR is zero in the RDG approximation because coupling is neglected and the spherical monomers thus cannot alter the polarization state of the incident light upon scattering into the backward direction. Indeed, the uniform internal-field approximation in RDG means that spherical monomers cannot alter the (linear) polarization state of the incident light upon scattering into *any* direction [36]. In this sense, one can regard nonzero values of the LDR as inherent consequences of coupling between monomers because coupling spoils the uniform internal-field approximation. Indeed, the λ^{-2} dependence in Fig. 5 can be explained qualitatively by dipole-dipole multiple scattering between monomers in the intermediate-field range via Eq. (81b) in [1]. It is understandable then that the superaggregate exhibits larger values of LDR than the canonical DLCA aggregate due to its more compact structure and larger size, hence more multiple scattering. Yet, the coating and restructuring of soot as it ages in the atmosphere further complicates attempts to attribute unexpectedly large LDR values to a given cause. A variety of studies have considered the effects of coating, such as [37, 38, 20] for example, and also find large values for the LDR that may exceed 10%.

There are a variety of explanations for such large LDR measurements. For example, the soot is usually aged on the order of days, and thus, has undergone significant chemical change, morphological restructuring, coating, and possibly coagulation with other classes of aerosol particles [38]. Mineral dust, which often exhibits large LDR, and other non-organic particulate matter may coexist with the soot at the measurement site. All of these factors can help explain the unexpectedly large LDR observations. A number of studies [37, 39, 38, 20] show how various modifications to pristine soot affect the LDR and related radiative properties, although many of the modifications employed vary substantially from one study to another. Yet, the success of these computational studies motivates further investigation.

5. Conclusion

This study reports the radiative properties of two specific types of soot fractal aggregates using both the conventional Rayleigh-Debye-Gans (RDG) approximation and the Superposition T-Matrix Method (STMM). Although the RDG is popular for light-scattering calculations due to its simplicity, we recall that the approximation neglects electromagnetic coupling, or multiple scattering, between monomers. The STMM, however, is a numerically exact solution in so far as the morphology and refractive index of the aggregate is accurately represented. Thus, the comparison above between STMM-calculated radiative properties and the RDG approximation offer a glimpse at the effects of coupling. Perhaps the most striking example is the LDR of Fig. 5. Other findings of this study are:

- The wavelength dependence of the soot refractive index from $\lambda = 300 - 1100$ nm does not spoil the power-law functionality of the differential scattering cross section in terms of $qR_{\mathrm{g,(c,s)}}$ expected from the RDG approximation, at least within 10% deviation.
- The scattering, extinction, and backscattering cross sections exhibit power-law functionality in terms of λ. Good agreement with the RDG approximation is found for the chain-like aggregate, while poorer agreement is seen for the superaggregate.
- The LDR for the canonical DLCA aggregate is within the range $0.1 - 2\%$ expected for low-sooting flames across the wavelengths considered, while the superaggregate exhibits approximately an order of magnitude greater LDR.
- Both aggregate types exhibit an approximate λ^{-2} functionality for the LDR, indicating stronger depolarization toward the UV/VIS end of the wavelength range.

Acknowledgements

The authors gratefully acknowledge funding from ONERA and the PROMETE project, the doctoral school Sciences mécaniques et énergétiques, matériaux et géosciences (SMEMAG), the National Science Foundation (1665456) and the Air Force Office of Scientific Research (FA9550-19-1-0078). The authors are grateful for helpful discussions with Jérôme Yon, Nicolas Riviere, Franck Enguehard, Alain Miffre, Michael Mishchenko, Anouar Soufiani, Laurent Soucasse, and Daniel Mackowski.

References

[1] C. M. Sorensen, Light scattering by fractal aggregates: A review, Aerosol Sci. Technol. 35 (2001) 648–687.

[2] C. M. Sorensen, A. Chakrabarti, The sol to gel transition in irreversible particulate systems, Soft Matter 7 (2011) 2284–2296.

[3] C. M. Sorensen, W. Kim, D. Fry, D. Shi, A. Chakrabarti, Observation of soot superaggregates with a fractal dimension of 2.6 in laminar acetylene/air diffusion flames, Langmuir 19 (2003) 7560–7563.

[4] S. P. Kearney, F. Pierce, Evidence of soot superaggregates in a turbulent pool fire, Combust. Flame 159 (2012) 3191–3198.

[5] W. Kim, C. M. Sorensen, A. Chakrabarti, Occurance of soot aggregates with a fractal dimension of 2.6 in heavily sooting laminar diffusion flames, Langmuir 20 (2004) 3969–3973.
[6] R. Dhaubhadel, F. Pierce, A. Chakrabarti, C. M. Sorensen, Hybrid superaggregate morphology as a result of aggregatation in a cluster dense aerosol, Phys. Rev. E 73 (2006) 011404.
[7] W. G. Kim, C. M. Sorensen, D. Fry, A. Chakrabarti, Soot aggregates, superaggregates and gel-like networks in laminar diffusion flames, J. Aerosol Sci. 37 (2006) 386–401.
[8] R. K. Chakrabarty, N. D. Beres, H. Moosmüller, S. China, C. Mazzoleni, M. K. Dubey, L. Liu, M. I. Mishchenko, Soot superaggregates from flaming wildfires and their direct radiative forcing, Scientific reports 4 (2014) 5508.
[9] R. K. Chakrabarty, H. Moosmüller, M. A. Garro, C. B. Stipe, Observation of superaggregates from a reversed gravity low-sooting flame, Aerosol Sci. Technol. 46.
[10] G. Roy, L. Bissonnette, C. Bastille, G. Vallée, Retrieval of droplet-size density distribution from multiple-field-of-view cross-polarized lidar signals: Theory and experimental validation, Appl. Optics 38 (1999) 5565–5581.
[11] L. R. Bissonnette, G. G. Roy, N. Roy, Multiple-scattering-based lidar retrieval: method and results of cloud probings, Appl. Optics 44 (2005) 5565–5581.
[12] S. P. Burton, J. W. Hair, M. Kahnert, R. A. Ferrare, C. A. Hostetler, A. L. Cook, D. B. Harper, T. A. Berkoff, S. T. Seaman, J. E. Collins, M. A. Fenn, R. R. Rogers, Observations of the spectral dependence of linear particle depolarization ratio of aerosols using NASA Langley airborne high spectral resolution lidar, Atmos. Chem. Phys. 15 (23) (2015) 13453–13473.
[13] A. Bescond, J. Yon, T. Girasole, C. Jouen, C. Roze, A. Coppalle, Numerical investigation of the possibility to determine the primary particle size of fractal aggregates by measuring light depolarization, J. Quant. Spectrosc. Radiat. Transfer 126 (2013) 130–139.
[14] X. Cao, G. Roy, N. Roy, R. Bernier, Comparison of the relationships between lidar integrated backscattered light and accumulated depolarization ratios for linear and circular polarization for water droplets, fog oil, and dust, Appl. Opt. 48 (2009) 4130–4141.
[15] T. Sakai, T. Nagi, Y. Zaizen, Y. Mano, Backscattering linear depolarization ratio measurements of mineral, sea-salt, and ammonium sulfate particles simulated in a laboratory chamber, Appl. Opt. 49 (2010) 4441–4449.
[16] M. D. Guasta, E. Vallar, O. Riviere, F. Castagnoli, V. Venturi, M. Morandi, Use of polarimetric lidar for the study of oriented ice plates in clouds, Appl. Opt. 45 (2006) 4878–4887.
[17] S. Groß, V. Freudenthaler, M. Wiegner, J. Gasteiger, A. Geiß, F. Schnell, Dual-wavelength linear depolarization ratio of volcanic aerosols: Lidar measurements of the Eyjafjallajökull plume over Maisach, Germany, Atmos. Environ. 48 (2012) 85–96.
[18] A. Boselli, S. Scollo, G. Leto, R. Z. Sanchez, A. Sannino, X. Wang, M. Coltelli, N. Spinelli, First volcanic plume measurements by an elastic/raman lidar close to the Etna summit craters, Font. Earth Sci. 6 (2018) 125.
[19] M. Haarig, A. Ansmann, H. Baars, C. Jimenez, I. Veselovskii, R. E. D. Althausen, Depolarization and lidar ratios at 355, 532, and 1064 nm and microphysical properties of aged tropospheric and stratospheric Canadian wildfire smoke, Atmos. Chem. Phys. 18 (2018) 11847–11861.
[20] F. Kanngießer, M. Kahnert, Calculation of optical properties of light-absorbing carbon with weakly absorbing coating: A model with tunable transition from film-coating to spherical-shell coating, J. Quant. Spectrosc. Radiat. Transfer 216 (2018) 17–36.
[21] R. Ceolato, F. Gaudfrin, O. Pujol, N. Riviere, M. J. Berg, C. M. Sorensen, Lidar cross-sections of soot fractal aggregates: Assessment of equivalent-sphere models, Journal of Quantitative Spectroscopy and Radiative Transfer 212 (2018) 39 – 44.
[22] L. Paulien, R. Ceolato, S. L, F. Enguehard, A. Soufani, Lidar-relevant radiative properties of soot fractal aggregate ensembles, J. Quant. Spectrosc. Radiat. Transfer.
[23] F. G. Pierce, Aggregation in Colloids and Aerosols, Ph.D dissertation, Kansas State University, 2007.
[24] D. W. Mackowski, M. I. Mishchenko, Calculation of the T matrix and the scattering matrix for ensembles of spheres, J. Opt. Soc. Am. A 13 (1996) 2266–2278.

[25] J. Yon, F. Liu, A. Bescond, C. Caumont-Prim, C. Rozé, F.-X. Ouf, A. Coppalle, Effects of multiple scattering on radiative properties of soot fractal aggregates, Journal of Quantitative Spectroscopy and Radiative Transfer 133 (2014) 374 – 381. doi:https://doi.org/10.1016/j.jqsrt.2013.08.022.
URL http://www.sciencedirect.com/science/article/pii/S0022407313003555

[26] M. I. Mishchenko, L. D. Travis, A. A. Lacis, Scattering, Absorption, and Emission of Light by Small Particles, Cambridge, 2002.

[27] H. Chang, T. T. Charalampopoulos, Determination of the wavelength dependence of refractive indices of flame soot, Proc. R. Soc. Lond. A 430 (1990) 577–591.

[28] M. I. Mishchenko, Electromagnetic Scattering by Particles and Particle Groups: An Introduction, Cambridge, 2014.

[29] C. M. Sorensen, J. Yon, F. Liu, J. Maughan, W. R. Heinson, M. J. Berg, Light scattering and absorption by fractal aggregates including soot, J. Quant. Spectrosc. Radiat. Transfer 217 (2018) 459–473.

[30] W. Heinson, C. Sorensen, A. Chakrabarti, A three parameter description of the structure of diffusion limited cluster fractal aggregates, Journal of colloid and interface science 375 (1) (2012) 65–69.

[31] R. A. Dobbins, C. M. Megaridis, Absorption and scattering of light by polydisperse aggregates, Applied optics 30 (33) (1991) 4747–4754.

[32] A. Comerón, C. Muñoz-Porcar, F. Rocadenbosch, A. Rodríguez-Gómez, M. Sicard, Current research in lidar technology used for the remote sensing of atmospheric aerosols, Sensors 17.

[33] G. G. Gimmestad, Reexamination of depolarization in lidar measurements, Appl. Opt. 47 (21) (2008) 3795–3802.

[34] M. Tesche, S. Gross, A. Ansmann, D. Müller, D. Althausen, V. Freudenthaler, M. Esselborn, Profiling of saharan dust and biomass burning smoke with multiwavelength polarization raman lidar at cape verde, Tellus 63B (2011) 649–676.

[35] G. David, B. Thomas, Y. Dupart, B. D'Anna, C. George, A. Miffre, P. Rairoux, UV polarization lidar for remote sensing new particles formation in the atmosphere, Opt. Ex. 22 (2014) A1009–A1022.

[36] M. Berg, C. M. Sorensen, A. Chakrabarti, Reflection symmetry of a sphere's internal field and its consequences on scattering: a microphysical approach, J. Opt. Soc. Am. A 25 (2008) 98–107.

[37] M. I. Mishchenko, J. M. Dlugach, L. Liu, Linear depolarization of lidar returns by aged smoke particles, Appl. Opt. 55 (2016) 9968–9973.

[38] L. Liu, M. I. Mishchenko, Scattering and radiative properties of morphologically complex carbonaceous aerosols: A systematic modeling study, Remote. Sens. 10 (2018) 1634.

[39] M. Kahnert, T. Nousiainen, H. Lindqvist, Models for integrated and differential scattering optical properties of encapsulated light absorbing carbon aggregates, Opt. Ex. 21 (7) (2013) 7974–7993.